ACS APPLIED NANO MATERIALS

www.acsanm.org Article

Ohmic Behavior in Metal Contacts to n/p-Type Transition-Metal Dichalcogenides: Schottky versus Tunneling Barrier Trade-off

Daniel Lizzit,* Pedram Khakbaz, Francesco Driussi, Marco Pala, and David Esseni

Cite This: *ACS Appl. Nano Mater.* 2023, 6, 5737−5746 Read Online

ACCESS | Metrics & More | Article Recommendations | Supporting Information

ABSTRACT: High contact resistance (R_C) between 3D metallic conductors and single-layer 2D semiconductors poses major challenges toward their integration in nanoscale electronic devices. While in experiments the large R_C values can be partly due to defects, ab initio simulations suggest that, even in defect-free structures, the interaction between metal and semiconductor orbitals can induce gap states that pin the Fermi level in the semiconductor band gap, increase the Schottky barrier height (SBH), and thus degrade the contact resistance. In this paper, we investigate, by using an in-house-developed ab initio transport methodology that combines density functional theory and nonequilibrium Green's function (NEGF) transport calculations, the physical properties and electrical resistance of several options for n-type top metal contacts to monolayer MoS_2, even in the presence of buffer layers, and for p-type contacts to monolayer WSe_2. The delicate interplay between the SBH and tunneling barrier thickness is quantitatively analyzed, confirming the excellent properties of the Bi−MoS_2 system as an n-type ohmic contact. Moreover, simulation results supported by literature experiments suggest that the Au−WSe_2 system is a promising candidate for p-type ohmic contacts. Finally, our analysis also reveals that a small modulation of a few angstroms of the distance between the (semi)metal and the transition-metal dichalcogenide (TMD) leads to large variations of R_C. This could help to explain the scattering of R_C values experimentally reported in the literature because different metal deposition techniques can result in small changes of the metal-to-TMD distance besides affecting the density of possible defects.

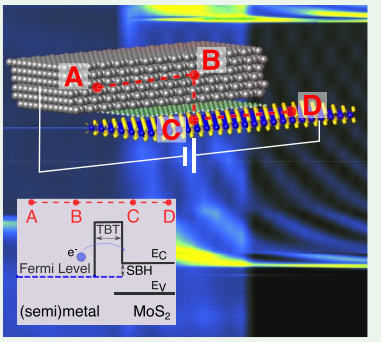

KEYWORDS: *contact resistance, Schottky barrier, tunneling barrier, buffer layers, quantum transport*

1. INTRODUCTION

Atomically thin 2D semiconductors belonging to the family of transition-metal dichalcogenides (TMDs) exhibit interesting physical properties stemming from the constituent elements and the structural arrangement. In particular, thanks to their extreme flexibility and large piezoresistance,[1] group VI TMDs like MoS_2 have great potential in many applications spanning from fast thermal sensors[2] to tactile sensing in soft robotics and electronic skin.[3] Moreover, TMDs have attracted remarkable attention for beyond silicon complementary metal oxide semiconductor (CMOS) circuits.[4,5] Indeed, despite the successful miniaturization of field-effect transistors (FETs) carried out for several decades, the scaling of silicon-based FETs to channel lengths in the sub-10-nm range appears almost prohibitive, mainly because of severe short channel effects and source-to-drain tunneling.[6,7] The monolayer MoS_2 has been identified as a promising baseline material for the ultimately scaled n-type FETs because the combination of subnanometer thickness and low dielectric constant improves the electrostatic integrity of the transistors. Moreover, a band gap larger than 1.7 eV and relatively large effective masses mitigate the source-to-drain tunneling.[8,9]

However, devices with high performances call for low-resistance ohmic contacts, which are still challenging to obtain.[10−15] Experimental results for metal−TMD contacts typically reported a large Fermi-level pinning (FLP) at the metal−TMD interfaces. In this respect, a measure of the FLP is the slope of the Schottky barrier height (SBH) versus the metal work function (WF). For vertical contacts to MoS_2 and WSe_2 obtained through electron-beam metal evaporation directly onto TMDs, such a slope has been experimentally reported to be as small as 0.09−0.3,[16−19] where a value close to 1 corresponds to a weakly interacting metal−TMD system, namely, to an unpinned interface. This strong FLP observed in the experiments may be partly due to complex phenomena like chalcogen or transition-metal atom vacancies, contamination of the semiconductor surface that may further induce surface reactions, chemical reactions with the metal contact, metal-induced MoS_2 strain, and also dislocation and atomic infiltration due to metal-atom deposition onto the semiconductor.[12,20−22] Metal-induced gap states (MIGSs) arising

Received: January 11, 2023
Accepted: March 22, 2023
Published: April 3, 2023

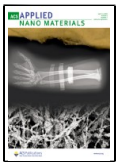

from the penetration of metal wave functions into the semiconductor layer,[22] however, can produce a significant SBH even for defect-free interfaces,[23−25] thus degrading the resulting contact resistance (R_C). Several experimental and simulation studies have reported a depinning of the Fermi level in metal−TMD contacts by inserting buffer layers [e.g., graphene, hexagonal boron nitride (hBN), silicon carbide, and thin oxides] between the metal and TMD, trying to zero the SBH.[17,18,22,24,26−33] However, the increased tunneling barrier thickness (TBT) adversely affects electron transmission between the metal and TMD, so that for many years the best reported R_C values have been in the range of kΩ μm.[28,32,33] Recent developments employing new materials and contact engineering schemes have allowed R_C to be decreased below 1 kΩ μm. This is the case, for instance, for metals like In and Sn, leading to a R_C to MoS_2 down to 190 Ω μm thanks to the reduced MoS_2 damage.[34] Moreover, it has been shown that semimetals like Bi and Sb, which can effectively suppress MIGSs due to the low density of states (DOS) at the Fermi level, can lead to good-quality n-type ohmic contacts to several TMDs, with a R_C value down to 123 Ω μm for the Bi−MoS_2 system.[35,36]

In this paper, we report ab initio calculations of R_C in metal− and semimetal−TMD heterostructures, even in the presence of buffer layers, obtained by extending the ab initio transport methodology proposed in ref 37. This work extends our previous studies on n-type contacts,[38] by analyzing more systems suitable for n- and p-type contacts and by providing a deeper analysis of the interplay between the TBT and SBH. We analyze Al and Sc in contact with MoS_2 by virtue of their low WFs of 4 and 3.6 eV,[16,39,40] respectively, which make them suitable candidates for n-type contacts. The semimetallic Bi is also investigated because of very promising recent experimental results.[35] Furthermore, we analyze a low-electron-affinity TMD, WSe_2, in contact with a high-WF metal, Au, as a material system for possible p-type ohmic contacts. The computational effectiveness of our simulation approach allowed us to address relatively large overlap regions between the (semi)metal and monolayer TMD, thus bridging the gap between the atomistic scale of the required modeling approach and the technologically relevant features in terms of dimensions for the metal−TMD vertical contacts.

2. COMPUTATIONAL METHODS

The *Quantum ESPRESSO* suite was used to investigate the electronic properties of several heterostructures made of MoS_2 (WSe_2) and metals or semimetals within density functional theory (DFT). All DFT simulations were performed by using orthorhombic supercells suited to perform transport calculations.[37] We investigated the behavior of vertical contacts with metals or semimetals having surface orientations exhibiting a hexagonal lattice [i.e., Al(111), Au(111), Sc(0001), and Bi(0001)], which are the metallic surfaces usually employed for either experimental or simulation studies concerning TMDs like MoS_2 and WSe_2.[19,24,26,29,35,41−46] The incommensurate in-plane lattice constants of, for instance, MoS_2 (3.16 Å) and metals [2.86 Å for Al(111) and 3.3 Å for Sc(0001)] may result in a Moiré pattern.[43,44] The periodicity of these superstructures has been experimentally measured for MoS_2 grown on Au(111),[43,44] Ag(111),[47] and Ag(110),[48] and it consists of several MoS_2 unit cells. In order to obtain a computationally manageable size of the supercell, ab initio simulations invariably imply a strain in MoS_2, in the metal, or in both materials. In this respect, experimental observations for MoS_2 grown on Au(111),[43,44,49] Ag(111),[42] and Gr-Ir(111)[50] have shown an MoS_2 lattice constant (averaged over several squared nanometers) very close to that of the unstrained MoS_2 (i.e., namely, about 3.16 Å[47,51]). Therefore, in our ab initio simulations the metal layer is forced to be commensurate with the unstrained MoS_2 (or WSe_2), as described in the Supporting Information section S2, which is consistent with previous studies.[24,26] Indeed, a strain up to a few percent does not significantly affect the electronic structure of the metals at the Fermi energy.[24] For the Al−MoS_2 and Au−WSe_2 contacts, the orthorhombic supercell is obtained by matching a 2 × 2 (111) metal surface of a six-layer crystal to a $\sqrt{3} \times \sqrt{3}$ MoS_2 unstrained monolayer supercell (Figure 1a), leading to lattice mismatches of about 4.3% and 1.8%, respectively. The Sc−MoS_2 contacts are simulated by matching a 1 × 1 Sc unit cell with a (0001) surface orientation with a 1 × 1 MoS_2 unstrained monolayer unit cell (Figure 1c), resulting in a lattice mismatch of about 4.2%. For simulations with the semimetal Bi, a 2 × 2 supercell of three Bi layers (0001) has been matched to a $\sqrt{7} \times \sqrt{7}$ unstrained MoS_2 cell (Figure 6a). The lattice mismatch is about 5.4% (compressive strain on Bi atoms). Then, for all of the studied heterostructures, relaxation was used to reduce residual forces on the atoms.[45,52] More details are provided in the Supporting Information section S2. The spurious coupling along the z direction (Figure 3a) between the periodic replicas of the supercell was minimized by including a ∼1.5 nm vacuum region along z and by duly employing a dipole correction to cancel the artificial interaction between the dipole moments along the z direction.[53]

For the n-type contacts, the cutoff energy of plane-wave-based DFT calculations was set to 612 eV (45 Ry) for the Al and Sc contacts and to 571 eV (42 Ry) for the Bi contact to MoS_2. A 6 × 8 × 1 Monkhorst−Pack k-point grid was used in the calculation of Hamiltonians in the basis of plane waves by using scalar relativistic norm-conserving pseudopotentials. For p-type contacts, WSe_2 exhibits a strong spin−orbit interaction in the W 5d orbitals (different from MoS_2), which leads to a large spin splitting of the valence-band (VB) states of ∼460 meV.[54] Therefore, we included spin−orbit coupling (SOC) in DFT simulations by using fully relativistic norm-conserving pseudopotentials with a cutoff energy of 952 eV (70 Ry). The convergence criteria were set to less than 2.6 meV/Å (0.1 mRy/bohr) forces acting on each ion and a total energy difference smaller than 1.36×10^{-5} eV (1×10^{-6} Ry) between two subsequent iterations. For all simulations, we employed the Perdew−Burke−Ernzerhof-type generalized gradient approximation exchange-correlation functional with Grimme DFT-D3 van der Waals (vdW) corrections.

In order to extend the rigor of DFT calculations to transport properties, the conductance across the heterostructures (Figure 3) was calculated by employing the Green Tea code,[55] which employs an ab initio transport methodology based on the nonequilibrium Green's function (NEGF) approach presented in ref 37. Our method starts from the plane-wave DFT Hamiltonian computed by *Quantum ESPRESSO* and reduces the size of the Hamiltonian blocks by transforming first to the hybrid $x\mathbf{K}_{yz}$ space (consisting of real space along the transport direction x and plane waves in the (y, z) directions[56]) and then to a basis set consisting of unit-cell-restricted Bloch functions (URBFs). The URBFs are accurately chosen to properly sample the first Brillouin zones (BZs) of the materials under investigation. Originally conceived for homogeneous systems, the method in ref 37 has been extended to deal with the heterostructures simulated in this work (Figure 3), consisting of the (semi)metal, the metal−TMD vertical heterojunction (VHJ), and finally the 2D semiconductor. Thus, to connect the different materials, the corresponding Hamiltonians are connected as described in the Supporting Information section S1. Once the blocks of the Hamiltonian matrix in the reduced URBF basis have been determined, the transmission and conductance across the (semi)-metal−TMD contacts were calculated by using standard NEGF algorithms.

3. RESULTS AND DISCUSSION

3.1. *n*-Type Contacts to MoS_2: SBH versus TBT Trade-off. Figure 1a shows the Al−MoS_2 orthorhombic supercell used for DFT calculations. The distance between the S and Al

https://doi.org/10.1021/acsanm.3c00166
ACS Appl. Nano Mater. 2023, 6, 5737−5746

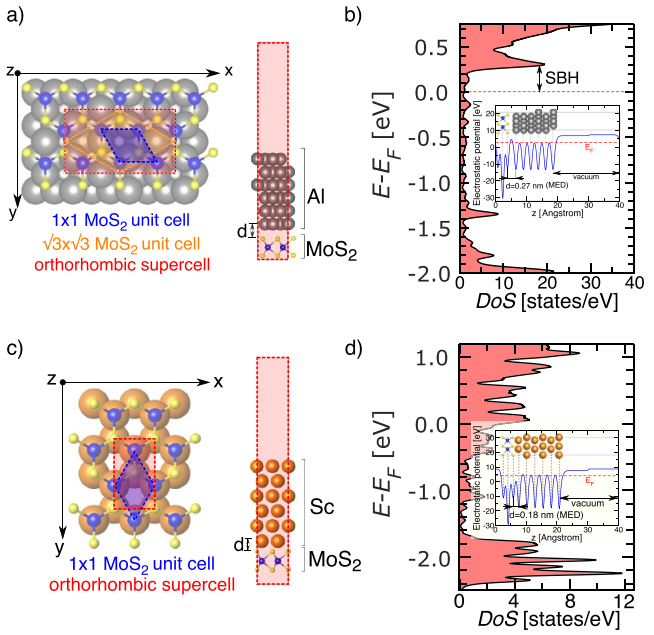

Figure 1. DFT simulations of the Al(Sc)−MoS_2 system. (a) Top and side views of the orthorhombic supercell used for the transport simulations of the Al−MoS_2 VHJ. (b) DOS projected on MoS_2 orbitals for the entire BZ and showing a SBH of about 0.3 eV. The inset shows that, thanks to the dipole correction placed at z = 30 Å, the electrostatic potential (averaged in the x−y plane) is flat in the vacuum region. (c and d) Orthorhombic supercell and DOS projected on the MoS_2 orbitals for the Sc−MoS_2 VHJ.

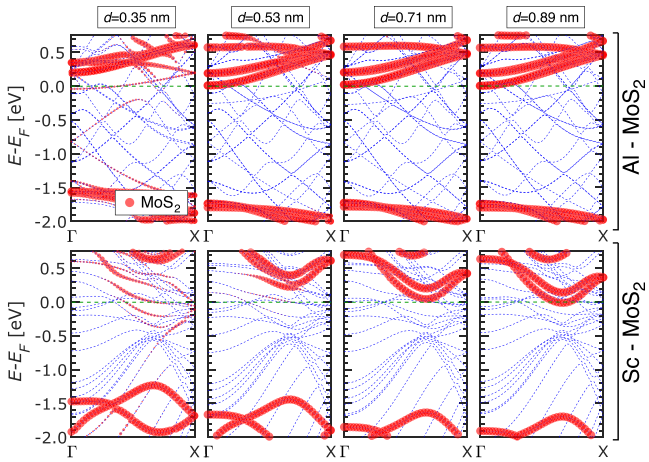

Figure 2. Electronic band structure (dashed blue lines) of the VHJs [i.e., Al(Sc)−MoS_2] for different distances d in Al−MoS_2 (top panel) and Sc−MoS_2 (bottom panel) and along the Γ−X path of the simulated orthorhombic supercell shown in parts a and c of Figure 1, respectively. Γ is at the center of the BZ, and X is the point on the rectangular BZ along k_x (Figures S3a,d and S4). Projected band structures on the MoS_2 states are shown with red circles, whose sizes are proportional to the weight of the states' projection.

atoms for the relaxed VHJ (i.e., the minimum energy distance, MED) is d = 0.27 nm, and it results in a large density of MIGSs, which are responsible for FLP inside the MoS_2 band gap and for a SBH of about 0.3 eV (Figure 1b). Such a value for the SBH is consistent with previously reported values.[24,52] Similar results have been obtained for the Sc−MoS_2 contact shown in Figure 1c, where the MED is lower and equal to d = 0.18 nm. This result is similar to the ∼0.2 nm obtained by using another 3d transition metal, namely, Ti, and it is related to the covalent nature of the metal−semiconductor bond.[57] In this case, the SBH cannot be easily determined because of the strong hybridization between MoS_2 and Sc, which is consistent with previous works,[12,26,45,46] as is also shown by the band structure plot in Figure S4.

Before dealing with contacts including buffer layers between the metal and MoS_2 (e.g., hBN or graphene), we investigated the trade-off between the TBT and SBH by varying the distance d between Al(Sc) and MoS_2. Therefore, we used these somewhat idealized simulations to assess the impact of a reduced MIGS density on the contact stack. Precise control of d in the subnanometer range is not technologically viable without resorting to buffer layers. Nonetheless, modulations of d are expected in the presence of Moiré superstructures, as shown by either experimental measurements[58] and DFT simulations.[59]

In Figure 2, we show the MoS_2 projected electronic structure for the Al−MoS_2 and Sc−MoS_2 VHJs, with d varying from 0.35 to 0.89 nm. For the Al−MoS_2 stack, a SBH of about 0.2 eV is still observed for d = 0.35 nm. Upon a further increase of the distance up to d = 0.89 nm, however, the projected MoS_2 conduction-band (CB) minimum is pulled down to the Fermi level (E_F); namely, the SBH is almost reduced to zero. The SBH at a relatively large distance d is in fairly good agreement with the Schottky−Mott rule considering an Al WF of 4 eV and an MoS_2 affinity of χ = 4.2 eV and also with the previously reported results obtained by increasing the distance between the metal and semiconductor.[41] For the Sc−MoS_2 VHJ, a sizable SBH is observed for a distance of up to 0.53 nm, whereas it becomes negligible for d = 0.71 nm and larger. Therefore, an increasing metal−MoS_2 distance can suppress the MIGS, thus depinning E_F and reducing the SBH. In this respect, to our best knowledge, only a very few experimental papers reported a SBH trend for metals in contact with MoS_2[60] (n-type contacts) or WSe_2[19] (p-type contacts), which follows the Schottky−Mott rule with a pinning factor close to 1. These results were obtained by the mechanical transfer of flat metal thin films onto a few MoS_2 layers[60] or by the use of sacrificial buffer layers with a relatively low desorption temperature,[19] to avoid direct metal deposition through evaporation, which could damage the TMD. Therefore, it is likely that the nonbonding vdW gap between the metal and semiconductor,[60] together with the possible presence of voids demonstrated in similar experiments,[61] can contribute to the reduction of the MIGS density due to a weakened interaction between the metal and TMD atoms,[41,62] as was, in fact, demonstrated by using scanning transmission electron microscopy (STEM) measurements in the Au−WSe_2 system.[19]

3.1.1. Transport across the Metal−Semiconductor Heterostructure. We investigated the impact of different SBHs and TBTs by using ab initio transport simulations based on the NEGF formalism in the ballistic limit. Transport simulations are performed by using the heterostructure illustrated in Figure 3a and consisting of a metal region, a VHJ region, and a free-standing TMD, corresponding to MoS_2 for n-type contacts. The barrier for carrier transport is given by the contact between the metal and TMD in the VHJ, as is pictorially illustrated in Figure 3b. In the framework of our simulation approach, it is important to identify the band structure of the TMD in the VHJ (see, for example, Figure 2), which sets the

https://doi.org/10.1021/acsanm.3c00166
ACS Appl. Nano Mater. 2023, 6, 5737−5746

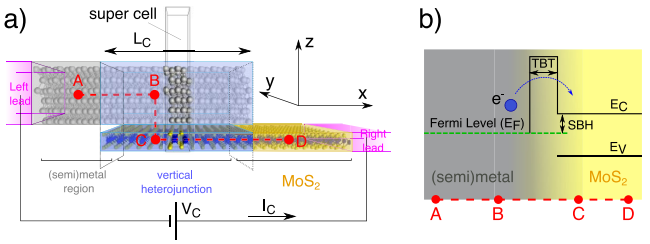

Figure 3. Metal− or semimetal−MoS_2 heterostructures analyzed in this paper for n-type contacts. (a) Sketch of the simulated heterostructure where *x*, *y*, and *z* denote the transport direction, the periodic or contact width direction, and the direction of the VHJ, respectively. The simulated heterostructure consists of three regions: the (semi)metal region at the left, the (semi)metal−MoS_2 VHJ in the center, and the MoS_2 region at the right. (b) Sketch of the band diagram along the same path depicted in part a, showing the TBT and SBH between the metal and MoS_2 in the VHJ.

alignment with the band structure of the free-standing TMD, as discussed in the Supporting Information section S1, thus neglecting any possible band bending in the TMD outside the VHJ region. It is thus understood that our simulation procedure allows us to investigate only the intrinsic resistance of the metal−TMD contact, namely, the resistance due to the interlayer tunneling in the VHJ, as shown in Figure 3b. Therefore, we did not address a self-consistent solution of the NEGF and Poisson equations.

For the reason above, transport simulations are performed only for distances d larger than 0.35 nm for the Al−MoS_2 contact and larger than 0.53 nm for the Sc−MoS_2 contact. Indeed, for smaller d values, it is impossible to identify in the VHJ a projection of the electronic states on MoS_2 resembling those of the free-standing material (Figure S4).

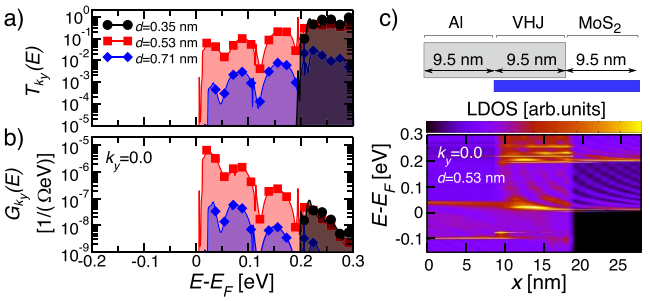

Figure 4. Simulation results for the Al−MoS_2 VHJ. The contact is sketched in part c and consists of an overlap between Al and MoS_2 of about 9.5 nm, corresponding to 10 orthorhombic unit cells (Figure 1a). The transmission and conductance are calculated for zero external bias V_C. (a) Transmission spectrum, $T_{k_y}(E)$, versus the energy calculated with the ab initio transport methodology described in the Computational Methods section. (b) Conductance spectrum calculated according to eq 1. (c) Energy-resolved LDOS for the Al−MoS_2 distance d = 0.53 nm. All results are shown for the transverse Bloch vector k_y = 0.

Figure 4a shows the transmission spectrum $T_{k_y}(E)$ (at a fixed lateral wave-vector k_y) across the Al−MoS_2 structure, calculated at the equilibrium (i.e., zero external bias), and for different Al−MoS_2 distances d. The system having d = 0.35 nm exhibits the largest transmission at the MoS_2 CB minimum, but the transmission is negligible at $E \sim E_F$ due to an SBH of about 0.2 eV. By increasing d to 0.53 nm, the SBH becomes negligible, but the transmission at the CB minimum is largely reduced by the TBT compared to the system with d = 0.35 nm. Upon a further increase in the distance d, the CB minimum remains close to the Fermi level but the increased TBT further decreases the transmission spectrum. To gain insight about the current drivability of the contacts, in Figure 4b, we show the corresponding linear conductance spectrum $G_{k_y}(E)$ for k_y = 0 [in units of 1/(Ω eV)], obtained through the Landauer formula:

$$G_{k_y}(E) = \frac{n_{sp}q^2}{h} T_{k_y}(E)\left(-\frac{df_0(E)}{dE}\right) \quad (1)$$

where $f_0(E)$ is the Fermi−Dirac function, the prefactor n_{sp} accounts for the spin degeneracy, and $T_{k_y}(E)$ is the equilibrium transmission spectrum. Finally, R_C per unit width is calculated by duly integrating over the Bloch vector k_y:

$$\frac{1}{R_C} = \frac{1}{2\pi}\int_{k_y}\left[\int_{-\infty}^{+\infty} G_{k_y}(E)\,dE\right]dk_y \quad (2)$$

It is clear from Figure 4b that the benefits of the large electronic transmission at d = 0.35 nm are frustrated by the corresponding SBH, namely, by the fact that large transmission occurs at energies well above the Fermi level. Similar results were found for the Sc−MoS_2 contact and are reported in Figure S7.

3.1.2. Buffer Layers in Metal−Semiconductor Contacts and Calculated R_C. An ultrathin buffer layer is a technologically viable means to modulate the metal−MoS_2 distance and reduce the density of MIGSs. It has been reported, for example, that a graphene buffer layer in an Ag−MoS_2 contact can decrease the SBH from 300 to 190 meV due to charge transfer from Ag to graphene.[27] Moreover, graphene buffer layers are also effective in reducing the SBH in Ti−MoS_2[28] and Ni−MoS_2[29] contacts. Metal oxides have also been used as buffer layers. A ZnO layer in Ti−MoS_2 contacts improves the slope of the SBH versus metal WF from 0.02 to 0.43,[30] while Al_2O_3 and TiO_2 buffer layers in Ti−MoS_2 can decrease the effective SBH from 0.18 eV to respectively 0.13 and 0.09 eV.[31] Experimental results have also been reported for ultrathin TiO_2 layers between Ti, Au, Cu, and Pt metals and MoS_2, showing an improved sensitivity of the SBH to the metal WF.[18] Also, 2D insulating materials, such as hBN, have been used as buffer layers in Ni−MoS_2 contacts, reducing the SBH from 158 to 31 meV,[32] and in Co−MoS_2 contacts, leading to a SBH of 15 meV.[63] Moreover, also few-layer TMDs like $MoSe_2$, WSe_2, and $ReWSe_2$ have been used as buffer layers in Ti−MoS_2 contacts, reducing the SBH to ∼25 meV.[33]

We investigated the impact of hBN and graphene buffer layers on Al−MoS_2 and Sc−MoS_2 contacts by using our atomistic modeling framework. DFT calculations show that both buffer layers separate Al from MoS_2 by approximately the same distance $d \sim$ 0.7 nm, which can effectively suppress the formation of MIGSs (Figure S5). While simulation results obtained by inserting hBN between Al and MoS_2 predict a SBH of ∼10 meV, which is consistent with experiments,[63,64] the results are substantially different when graphene is employed. Indeed, graphene appears to be unable to reduce the SBH, which instead increases from about 300 meV for Al−MoS_2 at the MED to 540 meV, as shown in the Supporting

https://doi.org/10.1021/acsanm.3c00166
ACS Appl. Nano Mater. 2023, 6, 5737−5746

Information section S4. This behavior can be explained thanks to the charge transfer that takes place between Al and Gr, which prevents electron charging of MoS_2. It is worth mentioning that also other DFT simulation studies, including different metals to contact MoS_2 (e.g., Au and Pt), show that the SBH is increased by using a graphene buffer layer.[65] On the other hand, in the Ag−MoS_2 and Ti−MoS_2 contacts, both experiments[27,28] and simulations[65] show a SBH reduction induced by the insertion of a graphene buffer layer. These differences are ascribed to the graphene−metal interaction, which strongly depends on the metal atomic species.[65] Because of the large observed SBH, we will not further investigate the properties of the Al−MoS_2 contact with a graphene buffer layer.

Figure 5 reports the simulated R_C versus contact length, L_C, for different contact options corresponding to Al and Sc. In the

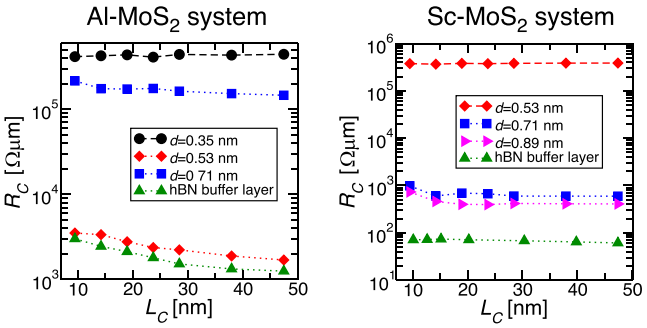

Figure 5. R_C for the Al−MoS_2 and Sc−MoS_2 systems with or without a hBN buffer layer and for different contact lengths L_C.

ballistic transport framework employed in this work, the conductance is expected to be independent of the system length,[66] and hence also independent of L_C, unless L_C is involved in resonance effects, possibly affecting the electronic transmission. For the Sc−MoS_2 contacts, R_C is practically independent of L_C for the options shown in Figure 5 (right). For the Al−MoS_2 contacts in Figure 5 (left), where R_C decreases at larger L_C, we verified that the local density of states (LDOS) of the Al−MoS_2 overlap region exhibits L_C-dependent resonance peaks at energies close to the Fermi level (Figure S9), which results in a significant sensitivity to L_C of the electronic transmission and R_C. The R_C dependence on L_C may also be expected in the presence of scattering centers distributed in the contact area, and a contact current proportional to L_C has been reported in simulations accounting for inelastic scattering.[67] Finally, in a diffusive transport regime, R_C is inversely proportional to the contact length as long as L_C is small compared to the transfer length.[68] However, the inclusion of scattering effects goes beyond the scope of this work.

Figure 5 shows that R_C changes in a wide range depending on the SBH and TBT, and Table 1 summarizes the SBH, TBT, and R_C values calculated for $L_C \sim 40$ nm. As can be seen, the low metal WF of Sc and the use of an hBN buffer layer result in the absence of a Schottky barrier, which is in qualitative agreement with ref 46. This can be explained in terms of a weakened metal−TMD interaction that suppresses the FLP and of the reduced metal WF due to hBN adsorption and resulting from the Pauli pushback effect.[24,46] The corresponding R_C value outperforms all of the other contact options explored in this section and should be identified as a very promising option in the quest for ohmic metal/2D material contacts.

Table 1. Calculated R_C for the Different Metal−MoS_2 Systems Investigated in This Paper

type	TBT (nm)	SBH (meV)	R_C at L_C = 40 nm (Ω μm)
		Al−MoS_2	
d = 0.35 nm	0.35	198	420 × 10^3
d = 0.53 nm	0.53	10	1.8 × 10^3
d = 0.71 nm	0.71	21	150 × 10^3
d = 0.89 nm	0.89	16	
w/hBN	0.71	9	1.3 × 10^3
w/Gr	0.69	540	>10^9
		Sc−MoS_2	
d = 0.53 nm	0.53	200	370 × 10^3
d = 0.71 nm	0.71	44	570
d = 0.89 nm	0.89	0	400
w/hBN	0.53	0	64

3.1.3. Semimetallic Bi to Reduce the MIGS. Very recently, it was experimentally shown that the semimetal Bi can provide an n-type ohmic contact to MoS_2 thanks to the low WF and the strong suppression of MIGSs enabled by the low DOS of Bi at the Fermi level.[35] We here report ab initio simulations of the resistance for the Bi−MoS_2 system illustrated in Figure 6.

After the structural optimization carried out as described in the Computational Methods section, the MED between the Bi and S layers amounts to 3.2 Å, which is in very good agreement with the value of 3.4 Å reported in ref 35. The MoS_2 projected electronic structure for the Bi−MoS_2 VHJ at the MED is shown in Figure 6c, where the green line identifies the branch corresponding to the CB minimum of the isolated MoS_2, which is, in fact, located in $[^1/_3(2\pi/a_x),0]$ for the orthorhombic supercell of Figure 6a. In transport simulations, such a green branch is used to set the energy alignment with the free-standing MoS_2 in the rightmost region of Figure 3a. As can be seen in Figure 6c, at the MED, there exists an energy branch crossing the Fermi level, corresponding to MIGSs that pin the Fermi level below the MoS_2 CB minimum. Due to the SBH of about 70 meV, in the MED case, the electrical behavior of the contact is not ohmic and the simulated R_C is about 4.5 kΩ μm, which is much larger than the value of 123 Ω μm experimentally reported for the Bi−MoS_2 contact.[35]

The possible presence of adsorbates between Bi and MoS_2 during the fabrication process and also misalignments between the Bi and MoS_2 layers may result in small uncertainties in the actual Bi−MoS_2 distance of the fabricated samples. Therefore, we investigated the influence on R_C of Bi−MoS_2 distances slightly larger than the MED, namely, d = 4.0, 4.5, and 5.3 Å. The band structures corresponding to the simulated d values are shown in parts d−f of Figure 6, respectively, where it can be seen that the increased Bi−MoS_2 distance can effectively suppress the MIGSs and lead to practically negligible SBHs for d = 4.0, 4.5, and 5.3 Å. The transmission across the VHJ, however, degrades by increasing d due to an increased TBT, so that Figure 6g reveals that the calculated R_C has a minimum for d = 4.5 Å, apparently resulting in the best compromise between the SBH and TBT.

Simulations in Figure 6g also suggest that R_C is dominated by the carrier injection across the VHJ, with the ballistic resistance of the MoS_2 region being much lower than R_C. This implies that the inclusion of inelastic scattering mechanisms, such as the electron−phonon interaction, could further

https://doi.org/10.1021/acsanm.3c00166
ACS Appl. Nano Mater. 2023, 6, 5737−5746

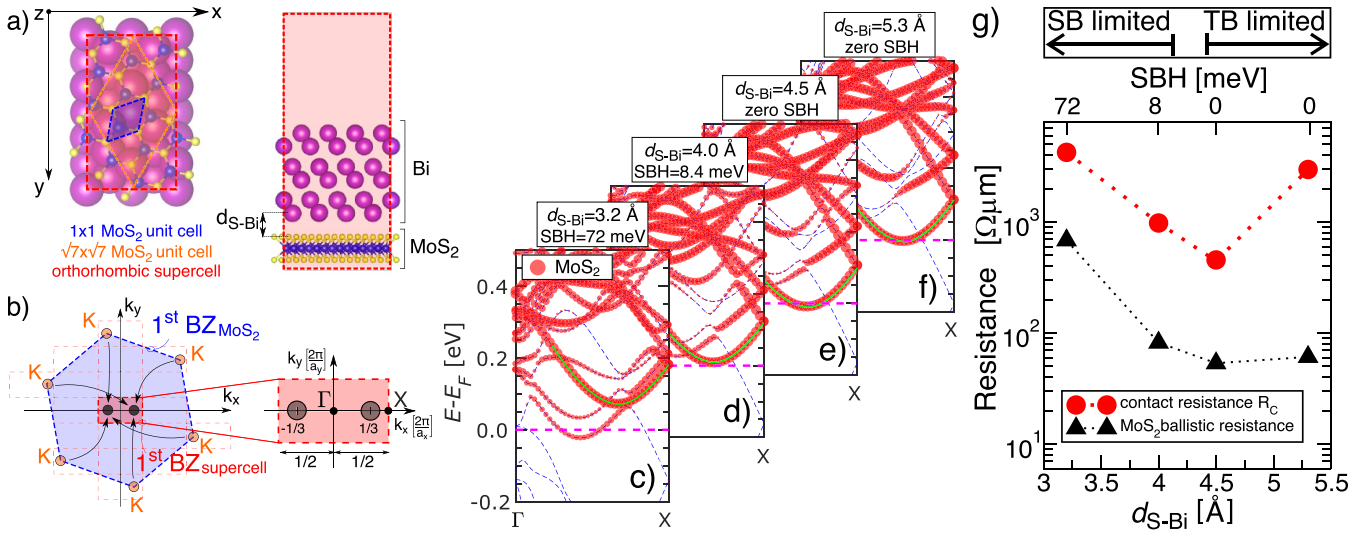

Figure 6. (a) Bi−MoS_2 VHJ simulated in this work. (b) Hexagonal first BZ for the primitive MoS_2 unit cell (blue hexagon) with K points at the corners of the BZ. Arrows show the back-folding of the high-symmetry points at the points $[\pm^1/_3(2\pi/a_x),0]$ in the BZ of the orthorhombic supercell (red rectangle) used in DFT simulations. (c−f) Electronic structure projected on MoS_2 zoomed in an energy range close to the CB minimum. Simulation results are obtained at (c) d = 3.2 Å (MED), (d) d = 4.0 Å, (e) d = 4.5 Å, and (f) d = 5.3 Å. The sizes of the red circles are proportional to the weight of the projection on MoS_2. Green lines are guides for the eyes to show the CB branch corresponding to the CB minimum of free-standing MoS_2 and with a minimum at $k_x = {}^1/_3[2\pi/a_x]$. (g) Resistance values for the Bi−MoS_2 contact having $L_C \sim 40$ nm. R_C (red circles) versus Bi−MoS_2 distance d, with the top horizontal axis reporting the corresponding SBH values. The ballistic resistance for MoS_2 (black triangles) is also shown for comparison, and it varies with d due to the change in the distance between the MoS_2 CB minimum and the Fermi level, which, in turn, affects the electron density and transverse modes in MoS_2. The experimental R_C from ref 35 is 123 Ω μm.

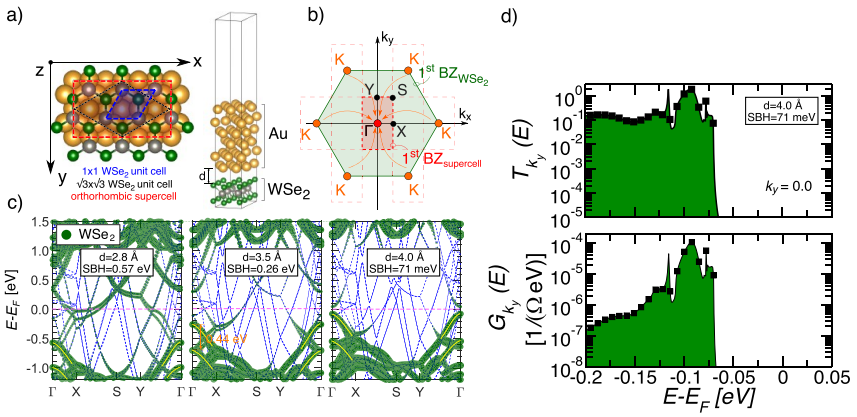

Figure 7. (a) Top and side views of the Au−WSe_2 VHJ for p-type contact with the simulated orthorhombic supercell (red rectangle). (b) BZ for the primitive WSe_2 unit cell (green hexagon) with the corresponding high-symmetry points back-folding on the orthorhombic supercell (red rectangle) shown by arrows. (c) Electronic structure (dashed line) and projection on WSe_2 orbitals (green circles) along the high-symmetry points shown in part b. Simulation results are obtained at the MED (d = 2.8 Å) and for d = 3.5 and 4.0 Å. Yellow lines are guides for the eyes and indicate the position of the top of the VB together with a spin splitting of ∼0.46 eV due to the strong SOC. (d) Transmission and conductance spectra calculated by using eq 1 for a tranverse wavevector k_y = 0.0 and considering a contact length $L_C \sim 10$ nm.

decrease R_C, enhancing the opening of additional tunneling paths across the VHJ and thus improving the agreement between our simulations and the R_C experimentally reported in ref 35, as shown in our recent work.[38] A similar effect of the electron−phonon scattering was previously reported in similar systems.[67]

Finally, we notice that our simulations predict a non-monotonic dependence of R_C on the metal−MoS_2 distance even for the Al−MoS_2 system, as can be seen in Table 1, because this is a fundamental behavior stemming from the opposite influence that the distance d has on the Schottky and on the tunneling barriers. The interplay between the two barriers is paramount for the overall R_C and has been illustrated throughout this paper.

3.2. p-Type Contact to WSe_2. By virtue of the large MoS_2 ionization energy obtained in this work from DFT simulations ($\chi + E_{GAP} \sim 5.9$ eV), which matches with previous DFT calculations[69] and is consistent with the 5.8 eV obtained from photoemission spectra,[70] contacting the MoS_2 VB is a very challenging problem. Hence, lower-ionization-energy TMDs, such as WSe_2 ($\chi + E_{GAP} \sim 4.86$ eV), and high-WF metals, such as Au (WF ∼ 5.3 eV), are better candidates for p-type ohmic contacts.[19] The SOC is large in heavy 5d elements and leads to a spin splitting of the VB maximum in WSe_2 of ∼0.46 eV, as experimentally observed through angle-resolved photoemission spectroscopy measurements.[54,71] Therefore, we included SOC in our DFT calculations, and this has a significant impact on

https://doi.org/10.1021/acsanm.3c00166
ACS Appl. Nano Mater. 2023, 6, 5737−5746

the VB maximum position with respect to the FL, and hence on the SBH for hole injection in the vertical contact.[72]

Figure 7a shows the simulated orthorhombic unit cell where, after relaxation of the atomic positions, the MED for the Au−WSe_2 contact is d = 0.28 nm. This value agrees with previously reported calculations[72] and matches well with the $d \sim 0.30$ nm estimated by STEM measurements for Au evaporated on WSe_2.[19] Figure 7c shows that the DFT results with SOC interaction reproduce well the splitting of the VB maximum experimentally reported for WSe_2 of ∼0.46 eV.[54,71] For the MED value, Figure 7c shows that DFT simulations predict a large p-type SBH of 0.57 eV due to MIGSs, as confirmed by the projected DOS in Figure S10. Such a large SBH is in qualitative agreement with the fact that, in recent results for a monolayer WSe_2 FET with Au contacts thermally evaporated directly onto WSe_2,[19] the drain-to-source current versus gate voltage characteristics were found to be almost flat, which authors ascribed to a large FLP in the contacts.

Figure 7c shows also that, similar to the results reported for n-type contacts, even in the Au and WSe_2 system, a slight increase of the Au−WSe_2 distance results in a drastic reduction of the SBH for holes to ∼70 meV for d = 0.40 nm. Such a behavior has also been experimentally observed for the same contact stack when a metal deposition process that relies on the evaporation of Au on a sacrificial Se buffer layer placed on top of WSe_2 is employed.[19] In this system, STEM measurements have revealed that an increased Au−WSe_2 distance from $d \sim 0.30$ to 0.38 nm could reduce the SBH to ∼60 meV and lead to a drain-to-source current modulation of several orders of magnitude as a function of the gate voltage, as opposed to the almost flat behavior reported for a smaller Au−WSe_2 distance of $d \sim 0.30$ nm.[19] Transport simulations, whose transmission and conductance spectra are shown in Figure 7d, predict that, for the Au−WSe_2 system with a distance d = 0.40 nm, R_C amounts to 7.5 kΩ μm, which is a value comparable to that reported for a five-layer WSe_2 in contact with Au.[19]

4. CONCLUSIONS

We used an in-house-developed ab initio transport methodology to investigate several material options for an n-type contact to a monolayer MoS_2, and we extended the analysis also to p-type contacts by studying the Au−WSe_2 system. Our results examined quantitatively the trade-off between the SBH and TBT either in idealized conditions, where the distance between the metal and TMD was increased beyond the MED identified by the DFT simulations, or in technologically feasible options, where a graphene or an hBN buffer layer was inserted between the metal and monolayer MoS_2. According to our results, the distance between the (semi)metal and TMD is a key parameter that strongly affects the transport properties of the vertical contact because it has a large influence on the hybridization between (semi)metal and TMD orbitals and thus on the density of MIGSs.

Even in defect-free metal−TMD contacts, the suppression of MIGSs appears to be very challenging and, at the same time, indispensable in order to zero the SBH and attain ohmic behavior. Our simulations have identified the Sc−hBN−MoS_2 system as the one that, thanks to the low metal WF and suppression of the gap states, can lead to very promising values of R_C. We have also analyzed the Bi−MoS_2 system that has been very recently experimentally investigated. Within a slight uncertainty in the actual Bi−MoS_2 distance, our ab initio simulations confirm that the Bi−MoS_2 system can have a negligible SBH even without resorting to any buffer layer, in which case it has ohmic behavior and a low R_C well below 1 kΩ μm. Moreover, simulations results for the Au−WSe_2 p-type contacts agree quite well with very recent experimental findings in terms of the SBH and R_C.

The ab initio simulation framework developed in this paper can be naturally employed to investigate other technological options (in terms of metals and TMDs) in order to identify the most promising systems for low-resistance ohmic contacts to TMD materials.

■ ASSOCIATED CONTENT

Supporting Information

The Supporting Information is available free of charge at https://pubs.acs.org/doi/10.1021/acsanm.3c00166.

Additional details regarding the approach used to construct the Hamiltonians of the simulated heterostrucutures, procedures adopted to define and simulate the metal−TMD orthorhombic supercells, atomic structure of the simulated orthorhombic supercells, band structure for Al−MoS_2 with graphene and hBN buffer layers, transmission and conductance spectra for Al(Sc)−MoS_2 contacts, transmission resonance peaks for Al(Sc)−MoS_2 with a hBN buffer layer, and partial DOS for the Au−WSe_2 system (PDF)

■ AUTHOR INFORMATION

Corresponding Author

Daniel Lizzit − *Polytechnic Department of Engineering and Architecture, University of Udine, 33100 Udine, Italy;* orcid.org/0000-0002-5243-5888; Email: daniel.lizzit@uniud.it

Authors

Pedram Khakbaz − *Polytechnic Department of Engineering and Architecture, University of Udine, 33100 Udine, Italy;* orcid.org/0000-0002-7794-1904

Francesco Driussi − *Polytechnic Department of Engineering and Architecture, University of Udine, 33100 Udine, Italy;* orcid.org/0000-0003-2175-6977

Marco Pala − *Université Paris-Saclay, CNRS, C2N, F-91120 Palaiseau, France*

David Esseni − *Polytechnic Department of Engineering and Architecture, University of Udine, 33100 Udine, Italy*

Complete contact information is available at: https://pubs.acs.org/10.1021/acsanm.3c00166

Notes

The authors declare no competing financial interest.

■ ACKNOWLEDGMENTS

This work was supported by the Italian MIUR through the PRIN project "Five2D" (No. 2017SRYEJH) and the French ANR through the projects "2D-on-Demand" (No. ANR-20-CE09-0026) and "Tunne-2D" (No. ANR-21-CE24-0030). We thank Paolo Giannozzi for fruitful discussions about usage of the *Quantum ESPRESSO* suite.

■ REFERENCES

(1) Hosseini, M.; Elahi, M.; Pourfath, M.; Esseni, D. Strain-Induced Modulation of Electron Mobility in Single-Layer Transition Metal

Dichalcogenides MX_2 (M = Mo, W; X = S, Se). *IEEE Trans. Electron Devices* **2015**, *62*, 3192−3198.
(2) Khan, A. I.; Khakbaz, P.; Brenner, K. A.; Smithe, K. K.; Mleczko, M. J.; Esseni, D.; Pop, E. Large temperature coefficient of resistance in atomically thin two-dimensional semiconductors. *Appl. Phys. Lett.* **2020**, *116*, 203105.
(3) Park, Y. J.; Sharma, B. K.; Shinde, S. M.; Kim, M.-S.; Jang, B.; Kim, J.-H.; Ahn, J.-H. All MoS_2-Based Large Area, Skin-Attachable Active-Matrix Tactile Sensor. *ACS Nano* **2019**, *13*, 3023−3030.
(4) Iannaccone, G.; Bonaccorso, F.; Colombo, L.; Fiori, G. Quantum engineering of transistors based on 2D materials heterostructures. *Nat. Nanotechnol.* **2018**, *13*, 183−191.
(5) Cao, J.; Wu, Y.; Zhang, H.; Logoteta, D.; Zhang, S.; Pala, M. Dissipative transport and phonon scattering suppression via valley engineering in single-layer antimonene and arsenene field-effect transistors. *npj 2D Materials and Applications* **2021**, *5*, 1−8.
(6) Kawaura, H.; Sakamoto, T.; Baba, T. Observation of source-to-drain direct tunneling current in 8 nm gate electrically variable shallow junction metal−oxide−semiconductor field-effect transistors. *Appl. Phys. Lett.* **2000**, *76*, 3810−3812.
(7) Quhe, R.; Xu, L.; Liu, S.; Yang, C.; Wang, Y.; Li, H.; Yang, J.; Li, Q.; Shi, B.; Li, Y.; Pan, Y.; Sun, X.; Li, J.; Weng, M.; Zhang, H.; Guo, Y.; Xu, L.; Tang, H.; Dong, J.; Yang, J.; Zhang, Z.; Lei, M.; Pan, F.; Lu, J. Sub-10 nm two-dimensional transistors: Theory and experiment. *Phys. Rep.* **2021**, *938*, 1−72.
(8) English, C. D.; Smithe, K. K. H.; Xu, R. L.; Pop, E. Approaching ballistic transport in monolayer MoS_2 transistors with self-aligned 10 nm top gates. *2016 IEEE International Electron Devices Meeting (IEDM)*; IEEE, 2016; pp 5.6.1−5.6.4.
(9) Wu, F.; Ren, J.; Yang, Y.; Yan, Z.; Tian, H.; Gou, G.; Wang, X.; Zhang, Z.; Yang, X.; Wu, X.; Ren, T.-L. A 10 nm Short Channel MoS_2 Transistor without the Resolution Requirement of Photolithography. *Advanced Electronic Materials* **2021**, *7*, 2100543.
(10) Zheng, Y.; Gao, J.; Han, C.; Chen, W. Ohmic Contact Engineering for Two-Dimensional Materials. *Cell Reports Physical Science* **2021**, *2*, 100298.
(11) Ni, J.; Fu, Q.; Ostrikov, K. K.; Gu, X.; Nan, H.; Xiao, S. Status and prospects of Ohmic contacts on two-dimensional semiconductors. *Nanotechnology* **2022**, *33*, 062005.
(12) Wang, Y.; Chhowalla, M. Making clean electrical contacts on 2D transition metal dichalcogenides. *Nat. Rev. Phys.* **2021**, 1−12.
(13) Mootheri, V.; Arutchelvan, G.; Banerjee, S.; Sutar, S.; Leonhardt, A.; Boulon, M.-E.; Huyghebaert, C.; Houssa, M.; Asselberghs, I.; Radu, I.; Heyns, M.; Lin, D. Graphene based Van der Waals contacts on MoS_2 field effect transistors. *2D Materials* **2021**, *8*, 015003.
(14) Passi, V.; Gahoi, A.; Marin, E. G.; Cusati, T.; Fortunelli, A.; Iannaccone, G.; Fiori, G.; Lemme, M. C. Ultralow Specific Contact Resistivity in Metal−Graphene Junctions via Contact Engineering. *Advanced Materials Interfaces* **2019**, *6*, 1801285.
(15) Cusati, T.; Fiori, G.; Gahoi, A.; Passi, V.; Lemme, M. C.; Fortunelli, A.; Iannaccone, G. Electrical properties of graphene-metal contacts. *Sci. Rep.* **2017**, *7*, 5109.
(16) Das, S.; Chen, H.-Y.; Penumatcha, A. V.; Appenzeller, J. High Performance Multilayer MoS_2 Transistors with Scandium Contacts. *Nano Lett.* **2013**, *13*, 100−105.
(17) Kaushik, N.; Karmakar, D.; Nipane, A.; Karande, S.; Lodha, S. Interfacial n-Doping Using an Ultrathin TiO2 Layer for Contact Resistance Reduction in MoS_2. *ACS Appl. Mater. Interfaces* **2016**, *8*, 256−263.
(18) Kim, G.-S.; Kim, S.-H.; Park, J.; Han, K. H.; Kim, J.; Yu, H.-Y. Schottky Barrier Height Engineering for Electrical Contacts of Multilayered MoS_2 Transistors with Reduction of Metal-Induced Gap States. *ACS Nano* **2018**, *12*, 6292−6300.
(19) Kwon, G.; Choi, Y.-H.; Lee, H.; Kim, H.-S.; Jeong, J.; Jeong, K.; Baik, M.; Kwon, H.; Ahn, J.; Lee, E.; Cho, M.-H. Interaction-and defect-free van der Waals contacts between metals and two-dimensional semiconductors. *Nature Electronics* **2022**, *5*, 241−247.
(20) Parto, K.; Pal, A.; Chavan, T.; Agashiwala, K.; Yeh, C.-H.; Cao, W.; Banerjee, K. One-Dimensional Edge Contacts to Two-Dimensional Transition-Metal Dichalcogenides: Uncovering the Role of Schottky-Barrier Anisotropy in Charge Transport across MoS_2/Metal Interfaces. *Phys. Rev. Applied* **2021**, *15*, 064068.
(21) Zheng, X.; Calò, A.; Albisetti, E.; Liu, X.; Alharbi, A. S. M.; Arefe, G.; Liu, X.; Spieser, M.; Yoo, W. J.; Taniguchi, T.; Watanabe, K.; Aruta, C.; Ciarrocchi, A.; Kis, A.; Lee, B. S.; Lipson, M.; Hone, J.; Shahrjerdi, D.; Riedo, E. Patterning metal contacts on monolayer MoS_2 with vanishing Schottky barriers using thermal nanolithography. *Nature Electronics* **2019**, *2*, 17−25.
(22) Chen, R.-S.; Ding, G.; Zhou, Y.; Han, S.-T. Fermi-level depinning of 2D transition metal dichalcogenide transistors. *J. Mater. Chem. C* **2021**, *9*, 11407−11427.
(23) Kang, J.; Liu, W.; Sarkar, D.; Jena, D.; Banerjee, K. Computational Study of Metal Contacts to Monolayer Transition-Metal Dichalcogenide Semiconductors. *Phys. Rev. X* **2014**, *4*, 031005.
(24) Farmanbar, M.; Brocks, G. First-principles study of van der Waals interactions and lattice mismatch at MoS_2/metal interfaces. *Phys. Rev. B* **2016**, *93*, 085304.
(25) Guo, Y.; Liu, D.; Robertson, J. 3D Behavior of Schottky Barriers of 2D Transition-Metal Dichalcogenides. *ACS Appl. Mater. Interfaces* **2015**, *7*, 25709−25715.
(26) Fang, Q.; Zhao, X.; Yuan, L.; Wang, B.; Xia, C.; Ma, F. Non-invasively improving the Schottky barrier of MoS_2/metal contacts by inserting a SiC layer. *Phys. Chem. Chem. Phys.* **2021**, *23*, 14796−14802.
(27) Chee, S.-S.; Seo, D.; Kim, H.; Jang, H.; Lee, S.; Moon, S. P.; Lee, K. H.; Kim, S. W.; Choi, H.; Ham, M.-H. Lowering the Schottky barrier height by graphene/Ag electrodes for high-mobility MoS_2 field-effect transistors. *Adv. Mater.* **2019**, *31*, 1804422.
(28) Du, Y.; Yang, L.; Zhang, J.; Liu, H.; Majumdar, K.; Kirsch, P. D.; Ye, P. D. MoS_2 Field-Effect Transistors With Graphene/Metal Heterocontacts. *IEEE Electron Device Lett.* **2014**, *35*, 599−601.
(29) Leong, W. S.; Luo, X.; Li, Y.; Khoo, K. H.; Quek, S. Y.; Thong, J. T. L. Low Resistance Metal Contacts to MoS_2 Devices with Nickel-Etched-Graphene Electrodes. *ACS Nano* **2015**, *9*, 869−877.
(30) Jang, J.; Kim, Y.; Chee, S.-S.; Kim, H.; Whang, D.; Kim, G.-H.; Yun, S. J. Clean Interface Contact Using a ZnO Interlayer for Low-Contact-Resistance MoS_2 Transistors. *ACS Appl. Mater. Interfaces* **2020**, *12*, 5031−5039.
(31) Park, W.; Kim, Y.; Lee, S. K.; Jung, U.; Yang, J. H.; Cho, C.; Kim, Y. J.; Lim, S. K.; Hwang, I. S.; Lee, H.-B.-R.; Lee, B. H. Contact resistance reduction using Fermi level de-pinning layer for MoS_2 FETs. *2014 IEEE International Electron Devices Meeting*; IEEE, 2014; pp 1−5.
(32) Wang, J.; Yao, Q.; Huang, C.-W.; Zou, X.; Liao, L.; Chen, S.; Fan, Z.; Zhang, K.; Wu, W.; Xiao, X.; Jiang, C.; Wu, W.-W. High Mobility MoS_2 transistor with low Schottky barrier contact by using atomic thick h-BN as a tunneling layer. *Advanced materials* **2016**, *28*, 8302−8308.
(33) Andrews, K.; Bowman, A.; Rijal, U.; Chen, P.-Y.; Zhou, Z. Improved contacts and device performance in MoS_2 transistors using a 2D semiconductor interlayer. *ACS Nano* **2020**, *14*, 6232−6241.
(34) Kumar, A.; Schauble, K.; Neilson, K. M.; Tang, A.; Ramesh, P.; Wong, H.-S. P.; Pop, E.; Saraswat, K. Sub-200 Ω μm Alloyed Contacts to Synthetic Monolayer MoS_2. *2021 IEEE International Electron Devices Meeting (IEDM)*; IEEE, 2021; pp 7.3.1−7.3.4.
(35) Shen, P.-C.; Su, C.; Lin, Y.; Chou, A.-S.; Cheng, C.-C.; Park, J.-H.; Chiu, M.-H.; Lu, A.-Y.; Tang, H.-L.; Tavakoli, M. M.; Pitner, G.; Ji, X.; Cai, Z.; Mao, N.; Wang, J.; Tung, V.; Li, J.; Bokor, J.; Zettl, A.; Wu, C.-I.; Palacios, T.; Li, L.-J.; Kong, J. Ultralow contact resistance between semimetal and monolayer semiconductors. *Nature* **2021**, *593*, 211−217.
(36) Chou, A.-S.; Wu, T.; Cheng, C.-C.; Zhan, S.-S.; Ni, I.-C.; Wang, S.-Y.; Chang, Y.-C.; Liew, S.-L.; Chen, E.; Chang, W.-H.; Wu, C.-I.; Cai, J.; Wong, H.-S. P.; Wang, H. Antimony Semimetal Contact with Enhanced Thermal Stability for High Performance 2D Electronics.

https://doi.org/10.1021/acsanm.3c00166
ACS Appl. Nano Mater. 2023, 6, 5737−5746

2021 IEEE International Electron Devices Meeting (IEDM); IEEE, 2021; pp 7.2.1−7.2.4.
(37) Pala, M. G.; Giannozzi, P.; Esseni, D. Unit cell restricted Bloch functions basis for first-principle transport models: Theory and application. *Phys. Rev. B* **2020**, *102*, 045410.
(38) Lizzit, D.; Khakbaz, P.; Driussi, F.; Pala, M.; Esseni, D. Ab initio transport simulations unveil the Schottky versus Tunneling barrier trade-off in metal−TMD contacts. *2022 IEEE International Electron Devices Meeting (IEDM)*; IEEE, 2022; pp 28.2.1−28.2.4.
(39) Tran, R.; Li, X.-G.; Montoya, J. H.; Winston, D.; Persson, K. A.; Ong, S. P. Anisotropic work function of elemental crystals. *Surf. Sci.* **2019**, *687*, 48−55.
(40) Hasan, M.; Park, H.; Yang, H.; Hwang, H.; Jung, H.-S.; Lee, J.-H. Ultralow work function of scandium metal gate with tantalum nitride interface layer for n-channel metal oxide semiconductor application. *Appl. Phys. Lett.* **2007**, *90*, 103510.
(41) Gong, C.; Colombo, L.; Wallace, R. M.; Cho, K. The Unusual Mechanism of Partial Fermi Level Pinning at Metal−MoS_2 Interfaces. *Nano Lett.* **2014**, *14*, 1714−1720.
(42) Tumino, F.; Grazianetti, C.; Martella, C.; Ruggeri, M.; Russo, V.; Li Bassi, A.; Molle, A.; Casari, C. S. Hydrophilic Character of Single-Layer MoS_2 Grown on Ag(111). *J. Phys. Chem. C* **2021**, *125*, 9479−9485.
(43) Bana, H.; Travaglia, E.; Bignardi, L.; Lacovig, P.; Sanders, C. E.; Dendzik, M.; Michiardi, M.; Bianchi, M.; Lizzit, D.; Presel, F.; De Angelis, D.; Apostol, N.; Kumar Das, P.; Fujii, J.; Vobornik, I.; Larciprete, R.; Baraldi, A.; Hofmann, P.; Lizzit, S. Epitaxial growth of single-orientation high-quality MoS_2 monolayers. *2D Mater.* **2018**, *5*, 035012.
(44) Bruix, A.; Miwa, J. A.; Hauptmann, N.; Wegner, D.; Ulstrup, S.; Grønborg, S. S.; Sanders, C. E.; Dendzik, M.; Grubišić Čabo, A.; Bianchi, M.; Lauritsen, J. V.; Khajetoorians, A. A.; Hammer, B.; Hofmann, P. Single-layer MoS_2 on Au(111): Band gap renormalization and substrate interaction. *Phys. Rev. B* **2016**, *93*, 165422.
(45) Zhong, H.; Quhe, R.; Wang, Y.; Ni, Z.; Ye, M.; Song, Z.; Pan, Y.; Yang, J.; Yang, L.; Lei, M.; Shi, J.; Lu, J. Interfacial Properties of Monolayer and Bilayer MoS_2 Contacts with Metals: Beyond the Energy Band Calculations. *Sci. Rep.* **2016**, *6*, 1−16.
(46) Su, J.; Feng, L.; Zhang, Y.; Liu, Z. The modulation of Schottky barriers of metal-MoS_2 contacts via BN-MoS_2 heterostructures. *Phys. Chem. Chem. Phys.* **2016**, *18*, 16882−16889.
(47) Yousofnejad, A.; Reecht, G.; Krane, N.; Lotze, C.; Franke, K. J. Monolayers of MoS_2 on Ag(111) as decoupling layers for organic molecules. *Beilstein J. Nanotechnol* **2020**, *11*, 1062−1071.
(48) Bignardi, L.; Mahatha, S. K.; Lizzit, D.; Bana, H.; Travaglia, E.; Lacovig, P.; Sanders, C.; Baraldi, A.; Hofmann, P.; Lizzit, S. Anisotropic strain in epitaxial single-layer molybdenum disulfide on Ag(110). *Nanoscale* **2021**, *13*, 18789−18798.
(49) Tumino, F.; Casari, C. S.; Passoni, M.; Russo, V.; Li Bassi, A. Pulsed laser deposition of single-layer MoS_2 on Au(111): from nanosized crystals to large-area films. *Nanoscale Adv.* **2019**, *1*, 643−655.
(50) Ehlen, N.; Hall, J.; Senkovskiy, B. V.; Hell, M.; Li, J.; Herman, A.; Smirnov, D.; Fedorov, A.; Yu Voroshnin, V.; Di Santo, G.; Petaccia, L.; Michely, T.; Grüneis, A. Narrow photoluminescence and Raman peaks of epitaxial MoS_2 on graphene/Ir(111). *2D Materials* **2019**, *6*, 011006.
(51) Wilson, J.; Yoffe, A. The transition metal dichalcogenides discussion and interpretation of the observed optical, electrical and structural properties. *Adv. Phys.* **1969**, *18*, 193−335.
(52) Khakbaz, P.; Driussi, F.; Giannozzi, P.; Gambi, A.; Esseni, D. Simulation study of Fermi level depinning in metal-MoS_2 contacts. *Solid-State Electron.* **2021**, *184*, 108039.
(53) Giannozzi, P.; Andreussi, O.; Brumme, T.; Bunau, O.; Buongiorno Nardelli, M.; Calandra, M.; Car, R.; Cavazzoni, C.; Ceresoli, D.; Cococcioni, M.; Colonna, N.; Carnimeo, I.; Dal Corso, A.; de Gironcoli, S.; Delugas, P.; DiStasio, R. A.; Ferretti, A.; Floris, A.; Fratesi, G.; Fugallo, G.; Gebauer, R.; Gerstmann, U.; Giustino, F.; Gorni, T.; Jia, J.; Kawamura, M.; Ko, H.-Y.; Kokalj, A.; Küçükbenli, E.; Lazzeri, M.; Marsili, M.; Marzari, N.; Mauri, F.; Nguyen, N. L.; Nguyen, H.-V.; Otero-de-la Roza, A.; Paulatto, L.; Poncé, S.; Rocca, D.; Sabatini, R.; Santra, B.; Schlipf, M.; Seitsonen, A. P.; Smogunov, A.; Timrov, I.; Thonhauser, T.; Umari, P.; Vast, N.; Wu, X.; Baroni, S. Advanced capabilities for materials modelling with Quantum ESPRESSO. *J. Phys.: Condens. Matter* **2017**, *29*, 465901.
(54) Zhang, Y.; Ugeda, M. M.; Jin, C.; Shi, S.-F.; Bradley, A. J.; Martín-Recio, A.; Ryu, H.; Kim, J.; Tang, S.; Kim, Y.; Zhou, B.; Hwang, C.; Chen, Y.; Wang, F.; Crommie, M. F.; Hussain, Z.; Shen, Z.-X.; Mo, S.-K. Electronic Structure, Surface Doping, and Optical Response in Epitaxial WSe2 Thin Films. *Nano Lett.* **2016**, *16*, 2485−2491.
(55) Green Tea code available at https://github.com/marcopala/Green-Tea-.
(56) Pala, M. G.; Esseni, D. Full-band quantum simulation of electron devices with the pseudopotential method: Theory, implementation, and applications. *Phys. Rev. B* **2018**, *97*, 125310.
(57) Popov, I.; Seifert, G.; Tománek, D. Designing Electrical Contacts to MoS_2 Monolayers: A Computational Study. *Phys. Rev. Lett.* **2012**, *108*, 156802.
(58) Sørensen, S. G.; Füchtbauer, H. G.; Tuxen, A. K.; Walton, A. S.; Lauritsen, J. V. Structure and Electronic Properties of In Situ Synthesized Single-Layer MoS_2 on a Gold Surface. *ACS Nano* **2014**, *8*, 6788−6796.
(59) Zhang, Z.; Guo, Y.; Robertson, J. Reduced Fermi Level Pinning at Physisorptive Sites of Moire-MoS2/Metal Schottky Barriers. *ACS Appl. Mater. Interfaces* **2022**, *14*, 11903−11909.
(60) Liu, Y.; Guo, J.; Zhu, E.; Liao, L.; Lee, S.-J.; Ding, M.; Shakir, I.; Gambin, V.; Huang, Y.; Duan, X. Approaching the Schottky−Mott limit in van der Waals metal−semiconductor junctions. *Nature* **2018**, *557*, 696−700.
(61) Zheng, W.; Saiz, F.; Shen, Y.; Zhu, K.; Liu, Y.; McAleese, C.; Conran, B.; Wang, X.; Lanza, M. Defect-Free Metal Deposition on 2D Materials via Inkjet Printing Technology. *Adv. Mater.* **2021**, 2104138.
(62) Farmanbar, M.; Brocks, G. Controlling the Schottky barrier at MoS_2/metal contacts by inserting a BN monolayer. *Phys. Rev. B* **2015**, *91*, 161304.
(63) Cui, X.; Shih, E.-M.; Jauregui, L. A.; Chae, S. H.; Kim, Y. D.; Li, B.; Seo, D.; Pistunova, K.; Yin, J.; Park, J.-H.; Choi, H.-J.; Lee, Y. H.; Watanabe, K.; Taniguchi, T.; Kim, P.; Dean, C. R.; Hone, J. C. Low-Temperature Ohmic Contact to Monolayer MoS_2 by van der Waals Bonded Co/h-BN Electrodes. *Nano Lett.* **2017**, *17*, 4781−4786.
(64) Lizzit, D.; Khakbaz, P.; Driussi, F.; Pala, M.; Esseni, D. A study of metal-MoS_2 contacts by using an in-house developed ab-initio transport simulator. *Solid-State Electron.* **2022**, *194*, 108365.
(65) Chanana, A.; Mahapatra, S. Prospects of zero Schottky barrier height in a graphene-inserted MoS_2-metal interface. *J. Appl. Phys.* **2016**, *119*, 014303.
(66) Landauer, R. Spatial variation of currents and fields due to localized scatterers in metallic conduction. *IBM J. Res. Dev.* **1988**, *32*, 306−316.
(67) Szabó, A.; Jain, A.; Parzefall, M.; Novotny, L.; Luisier, M. Electron Transport through Metal/MoS_2 Interfaces: Edge- or Area-Dependent Process? *Nano Lett.* **2019**, *19*, 3641−3647.
(68) Gahoi, A.; Kataria, S.; Driussi, F.; Venica, S.; Pandey, H.; Esseni, D.; Selmi, L.; Lemme, M. C. Dependable Contact Related Parameter Extraction in Graphene−Metal Junctions. *Advanced Electronic Materials* **2020**, *6*, 2000386.
(69) Kim, H.-g.; Choi, H. J. Thickness dependence of work function, ionization energy, and electron affinity of Mo and W dichalcogenides from DFT and GW calculations. *Phys. Rev. B* **2021**, *103*, 085404.
(70) Keyshar, K.; Berg, M.; Zhang, X.; Vajtai, R.; Gupta, G.; Chan, C. K.; Beechem, T. E.; Ajayan, P. M.; Mohite, A. D.; Ohta, T. Experimental Determination of the Ionization Energies of MoSe2, WS2, and MoS2 on SiO2 Using Photoemission Electron Microscopy. *ACS Nano* **2017**, *11*, 8223−8230.
(71) Nguyen, P. V.; Teutsch, N. C.; Wilson, N. P.; Kahn, J.; Xia, X.; Graham, A. J.; Kandyba, V.; Giampietri, A.; Barinov, A.; Constantinescu, G. C.; Yeung, N.; Hine, N. D. M.; Xu, X.; Cobden,

https://doi.org/10.1021/acsanm.3c00166
ACS Appl. Nano Mater. 2023, 6, 5737−5746

D. H.; Wilson, N. R. Visualizing electrostatic gating effects in two-dimensional heterostructures. *Nature* **2019**, *572*, 220−223.
(72) Wang, Y.; Yang, R. X.; Quhe, R.; Zhong, H.; Cong, L.; Ye, M.; Ni, Z.; Song, Z.; Yang, J.; Shi, J.; Li, J.; Lu, J. Does p-type ohmic contact exist in WSe2−metal interfaces? *Nanoscale* **2016**, *8*, 1179−1191.

https://doi.org/10.1021/acsanm.3c00166
ACS Appl. Nano Mater. 2023, 6, 5737−5746